INTERNATIONAL ATOMIC ENERGY AGENCY
UNITED NATIONS EDUCATIONAL, SCIENTIFIC AND CULTURAL ORGANIZATION

INTERNATIONAL CENTRE FOR THEORETICAL PHYSICS
34100 TRIESTE (ITALY) - P.O.B. 586 - MIRAMARE - STRADA COSTIERA 11 - TELEPHONE: 2240-1
CABLE: CENTRATOM - TELEX 460392-I

H4.SMR/285 - 7

WINTER COLLEGE ON
LASER PHYSICS: SEMICONDUCTOR LASERS
AND INTEGRATED OPTICS

(22 February - 11 March 1988)

THE PHYSICS OF HETEROSTRUCTURE QUANTUM WELLS AND SUPERLATTICES

E. Towe
Dept. of Electrical Eng. & Computer Science
Massachusetts Institute of Technology
Massachusetts, USA

Abstract

We discuss the basic physics of heterostructure quantum wells and superlattices. The energy dispersion relations are presented as derived from a simple envelope function approximation based on a Kane-type energy band structure analysis.

1. Introduction

Developments in the field of crystal growth have led to advances in the field of photonics: the combined area of electro-optics, laser physics and non-linear optics. The impact of these advances on modern communication and computing technology cannot be understated. It has therefore become essential for workers in this field to have a basic understanding and an appreciation for some of the physics associated with the microstructures prepared by the new techniques for applications in photonics. In this paper, we aim at discussing the basic physics of practical quantum wells at a level accessible to the non-specialist. The specialized and detailed treatment of this subject can be found in some of the literature cited and in the references therein.

2. Fundamentals of Heterostructure Quantum Wells

The theoretical concept of a quantum well has been around since the early days of Quantum Mechanics. It has only been in recent years that experimental fabrication of quantum wells has been demostrated.

In the textbook case, an electronic carrier is confined within a well when it is in a region of space with low potential energy surrounded by walls of infinitely high potential energy. In this section, we will concern ourselves with practical quantum wells. The demonstration and achievement of this type of well is intimately linked with the science and technology of crystal growth. In recent years, crystal growth techniques [1] and processing methods have advanced to such a state that it is now routinely possible to obtain ultra-thin and structurally perfect solid films that exhibit quantum size effects (QSE). Quantum size effects become operative in solid layers when the film or surface depth dimension is comparable to the de Broglie wavelength ($\lambda = h/p \sim L_w$) of the

electronic particle or to its mean free path in the layer. These effects also lead to changes in some very basic physical quantities of the semiconductor. Such quantities as the Bohr radius and the Rydberg constant associated with impurity states acquire modified values in structures containing quantum wells. In the III-V semiconductor compounds, the Bohr radius then ranges from 10 to 500 Å with the corresponding effective Rydberg constants ranging from 100 meV to 1 meV.

When quantum size effects occur, they produce changes in the macroscopic electronic properties of the layer, film or surface. And it is these changes, particularly in the optical and electrical properties of the solid, that are exploited in the design of new semiconductor devices.

We begin by discussing carrier confinement in terms of the "particle-in-the-box" model. The implicit assumption in this model, however, is that the host heterostructures have parabolic conduction and valence bands in reciprocal space. This model has intuitive clarity and physical appeal, and for special cases of the type I semiconductor heterostructure, it gives reasonable quantitative results. It should, however, be viewed only as a first order computational tool.

The formation of a heterostructure quantum well involves the epitaxial growth of two semiconductor crystals with approximately the same lattice parameter but different band gap energies. In Fig. 1, we show the (Al,Ga)As and GaAs semiconductor heterostructure system. The GaAs material, which has a smaller band gap than the (Al,Ga)As, is sandwiched between two layers of the (Al,Ga)As material to form the quantum well.

The distribution of electronic carriers in a semiconductor with a quantum well is markedly different from that in the bulk crystal. The physical nature of the quantum well imposes a quasi two-dimensional behavior on the carriers. The energies, for example, that each carrier may have are quantized in a prescribed manner. The prescription of the

allowed energy levels is governed by quantum mechanics. In a quantum well, such as the one formed in the (Al,Ga)As/GaAs crystal system, one may determine the particular energies that are permitted for occupation by the carriers by solving the Schrödinger wave equation. The Hamiltonian (in the single particle approximation) that is used in this calculation is assumed to be separable in the cartesian coordinate system. Therefore, for the quantum wells shown in Fig. 2, the relevant component of the Hamiltonian would be the z-component which is normal to the epitaxial layer. The lateral component would give rise to the usual, unconfined Bloch carrier states.

We write down the Schrödinger equation to be solved for the problem in Fig. 2 as

$$-\frac{\hbar^2}{2m_e}\left[\frac{\partial^2}{\partial z^2}+\Delta E_c(z)\right]\Phi_{cn}(z)=E_{cn}\Phi_{cn}(z) \qquad (1)$$

where m_e is the electron effective mass and $\Delta E_c(z)$ is the conduction band discontinuity with a zero of energy at the conduction band edge. The E_{cn} are the eigen-energies and the $\Phi_{cn}(z)$ are the associated eigen-functions. The carrier effective mass, m_e, is to be distinguished in the GaAs and the (Al,Ga)As regions as m_{ew} and m_{eb}, respectively. This equation is written for the conduction band quantum well. An analogous equation can be written down for the valence band quantum well. In the valence band, however, the usual degeneracy of the bands for most III-V semiconductors at the Brillouin zone center, is lifted for quantum well structures. It is therefore necessary to take into account both the light- and heavy-holes. This will be explained in detail in a later section. In a later section we will also discuss another mechanism by which the valence band degeneracy is lifted.

For the two regions of Fig. 2, Eq. (1) can be split into two auxilliary parts; for region 2,

$$\frac{d^2\Phi_{cn}(z)}{dz^2} - \kappa^2\Phi_{cn}(z) = 0 \tag{2}$$

with the relevant solutions being

$$\Phi_{cn}(z) = Ae^{\kappa z} \qquad z < -L_w, \tag{3}$$

$$\Phi_{cn}(z) = De^{-\kappa z} \qquad z > L_w, \tag{4}$$

where

$$\kappa = \frac{\sqrt{2m_{eb}(\Delta E_c - E_{cn})}}{\hbar}. \tag{5}$$

A and D are arbitrary constants of integration. In region 1, the Schrödinger equation is

$$\frac{d^2\Phi_{cn}(z)}{dz^2} + k^2\Phi_{cn}(z) = 0 \tag{6}$$

and the solutions take the form

$$\Phi_{cn}(z) = B\cos kz + C\sin kz \qquad |z| \le L_w, \tag{7}$$

where

$$k = \frac{\sqrt{2m_{cw}E_{cn}}}{\hbar}. \tag{8}$$

The quantities B and C are the arbitrary constants of this integration . By requiring that the eigen-functions of Eqs. (3), (4) and (7) and their first derivatives be continuous at the hetero-interfaces, *i.e.*, at $z = \pm L_w$, we obtain the system of equations

$$\begin{pmatrix} -e^{-\kappa L_w} & \cos kL_w & -\sin kL_w & 0 \\ -\kappa e^{-\kappa L_w} & k\sin L_w & k\cos kL_w & 0 \\ 0 & \cos kL_w & \sin kL_w & -e^{-\kappa L_w} \\ 0 & -k\sin kL_w & k\cos L_w & \kappa e^{-\kappa L_w} \end{pmatrix} \begin{pmatrix} A \\ B \\ C \\ D \end{pmatrix} = 0. \tag{9}$$

From this system of equations, we derive the eigen-value conditions:

$$k\tan kL_w = \kappa \qquad A + D \neq 0,\ B \neq 0 \tag{10}$$

and

$$k\cot kL_w = -\kappa \qquad A - D \neq 0,\ C \neq 0. \tag{11}$$

These conditions cannot be satisfied simultaneously. Therefore, if at one time Eq. (10) is true, it can be shown that the corresponding eigen-state is

$$\Phi_{cn}(z) = (B\cos kL_w)e^{\kappa(z+L_w)} \qquad z < -L_w, \tag{12}$$

$$\Phi_{cn}(z) = B\cos kz \qquad |z| \le L_w, \tag{13}$$

$$\Phi_{cn}(z) = (B\cos kL_w)e^{-\kappa(z-L_w)} \qquad y > L_w. \tag{14}$$

This state is said to have *even parity*. On the other hand, when Eq. (11) is valid and Eq. (10) is not, the correct eigen-state is given by

$$\Phi_{cn}(z) = (-C\sin kL_w)e^{\kappa(z+L_w)} \qquad z < -L_w, \tag{15}$$

$$\Phi_{en}(z) = C \sin kz \qquad |z| < L_w, \tag{16}$$

$$\Phi_{en}(z) = (C \sin kL_w) e^{-\kappa(z-L_w)} \qquad z > L_w. \tag{17}$$

This state has *odd parity*.

Since the eigen-states of Eqs. (12-14) and Eqs. (15-17) represent bound electron states in the well, the arbitrary constants B and C can be determined by imposing a normalization condition

$$\int_{-\infty}^{\infty} |\Phi_{en}(z)|^2 dz = 1. \tag{18}$$

The eigen-energies, E_{en}, for the bound states in the quantum well are determined from Eq. (10) for n even and from Eq. (11) for n odd. From the definition of κ in Eq. (5) and k in Eq. (8) and the eigen-value conditions of Eq. (10) and Eq. (11), we can write a single eigen-value equation implicitly for the system as

$$\sqrt{\frac{m_{eb}}{m_{ew}}\left[\frac{V_o - E_n}{E_n}\right]} = \begin{cases} \tan\sqrt{(m_{ew}L_w^2 E_n)/(2\hbar^2)} \\ -\cot\sqrt{(m_{ew}L_w^2 E_n)/(2\hbar^2)} \end{cases} \tag{19}$$

where $V_o (= \Delta E_c)$ is the well depth, L_w is the well width. E_n is the n-th eigen-energy, m_{ew} and m_{eb} are the electron effective masses in the well and in the barrier, respectively. Eq. (19) can be transformed into dimensionless form by writing

$$\begin{aligned} \rho^2 &= (m_{eb}L_w^2 V_o)/2\hbar^2, \\ \xi^2 &= (m_{ew}L^2 E_n)/2\hbar^2. \end{aligned} \tag{20}$$

With this transformation, Eq. (19) becomes

$$\sqrt{\rho^2 - \frac{m_{eb}}{m_{ew}}\xi^2} = \begin{cases} \xi \tan\xi \\ -\xi \cot\xi. \end{cases} \tag{21}$$

Eq. (21) is now in a form that can be solved graphically. If we plot the left hand side of Eq. (21) as a function of ξ and the right hand side also as a function of ξ, the intersections specify values of ξ which are solutions to Eq. (21). By use of Eq. (20), we can then determine the eigen-energies E_n.

For a typical quantum well width of L_w=125 Å, we have plotted the solutions of Eq. (21) for the even eigen-states of a confined electron in a conduction band quantum well. These solutions are shown in Fig. 3. The electronic band parameters used are listed in Table 1. The complete set of eigen-energies for the $Al_{0.2}Ga_{0.8}As/GaAs/Al_{0.2}Ga_{0.8}As$ single well structure with a width of 125 Å is shown in Fig. 2.

Table 1: Electronic Band Parameters

$m_e(x) = (0.067 + 0.085x)m_0$	$m_{lh}(x) = (0.087 + 0.063x)m_0$
$m_{hh}(x) = (0.450 + 0.140x)m_0$	$m_0 = 9.109 \times 10^{-31}$ kg
$E_g(x) = 1.424 + 1.247x$ eV	$\Delta E_g = E_g(x) - E_g(0)$ eV
$\Delta E_c = 0.62\Delta E_g$	$\Delta E_v = 0.38\Delta E_g$
$V_0 = \Delta E_c(\Delta E_v)$	$L_w = 125$ Å
$x = 0.2$	

One of the most immediate consequences for optical transitions in a direct gap semiconductor containing quantum wells is that the energy of the transitions is shifted to higher energies as is shown in Fig. 4. This illustration shows the photoluminescence emission spectrum of a bulk GaAs layer contrasted against the emission spectrum emanating from a layer with (Al,Ga)As/GaAs quantum wells in it. One major optical

transition is from the first confined electron state in the conduction band to the first confined heavy-hole state in the valence band ($1e \rightarrow 1hh$). Another is the electron to light-hole transition ($1e \rightarrow 1lh$). The calculated transitions, using the simple particle-in-the-box model, agree with the experimentally-observed ones. The character of these transitions is shown schematically on an energy band diagram in Fig. 5. Notice the contrast with the transitions that occur in a bulk semiconductor.

3. Density of States for Quantum Well Structures

In bulk III-V compound semiconductors where the energy dispersion relations can be approximated as parabolic near the Brillouin zone center, the joint density of occupiable electronic states can be shown to be given by [2]

$$D_{vc}(E) = \frac{2}{8\pi^3}\int\int \frac{dS}{\nabla_k(E_c - E_v)}\bigg|_{E_c - E_v = E} = \frac{1}{2\pi^2}\left(\frac{2m_h m_e}{m_h + m_e}\cdot\frac{1}{\hbar^2}\right)^{3/2}\sqrt{E - E_g}. \qquad (22)$$

In quantum wells, the carriers are constrained to move in the plane parallel to the layers. If z is the direction of confinement, then motion is possible only in the $x - y$ plane. The joint density of states in this case is given by

$$D_{vc}(E) = \frac{2}{4\pi^2}\int \frac{dl}{\nabla_{k_{||}}(E_c - E_v)}\bigg|_{E_c - E_v = E}. \qquad (23)$$

The operator $\nabla_{k_{||}}$ is the directional second derivative of the energy difference-function parallel to the epi-layers. This joint density of states as given here is per unit range of energy per unit area. For a quantum well of width L_w, the joint density of states per unit range of energy per unit volume can be expressed as

$$D_{vc}(E) = \left(\frac{m_h m_e}{m_h + m_e}\right)\frac{1}{\pi\hbar^2 L_w}\sum_n u_{-1}(E - \Delta E_n) \qquad (24)$$

where $u_{-1}(E - \Delta E_n)$ is the unit step function and $\Delta E_n = E_{cn} - E_{vn}$ is the energy difference between two allowed conduction and valence band states.

We note that the confinement of carriers in the quantum well structure produces a different density of states function from that which is usual in a bulk crystal. The major differences stem from the energy independence of the two-dimensional density of states for a given energy range. Also, the two-dimensional density of states has a step-like functional dependence. The differences lead to markedly contrasting observable optical properties.

4. Multiple Quantum Wells and Superlattices

The major difference between a multiple quantum well system and a superlattice is the relative magnitude of the barrier layer thickness L_b, and its relationship to the wave function penetration depth L_p, in the barrier. In multiple quantum wells, the barrier thickness, L_b, is much larger than the wave function penetration depth L_p (*i.e.*, $L_b >> L_p$). Therefore, the wave functions of adjacent wells do not overlap, and the physical properties of the multiple quantum well system are those of an independent set of wells. Most of the physics of these systems can therefore be studied in a single quantum well and is not restricted to the multiple quantum well systems. As a practical matter though, the signal-to-noise ratio is much better in multiple quantum well systems for any given experiment on these structures. This is one of the main reasons for working with multiple quantum well structures rather than a single quantum well structure, and results from the N-fold increase in the density of states for multiple quantum wells.

In superlattices which, in principle, are any set of infinite, periodic layers, the barrier thickness, L_b, is much less than the wave function penetration depth L_p; this means that the wave functions of adjacent wells interact and the confined particles are delocalized. The physical properties of these structures therefore depend on the super periodicity superimposed on top of the lattice periodicity. The energy distribution of the delocalized carriers in the superlattice takes on a new form. The discrete energy distribution characteristic of isolated quantum well structures changes into mini-bands separated by mini-gaps.

5. The Envelope Function Approximation

In a preceding section we discussed carrier confinement in a single quantum well within the plane-wave matching framework. This one-band approximation technique works rather well for the (Al,Ga)As/GaAs heterostructure system, but it fails to fully account for the InAs-GaSb system [3] because it does not take into account the symmetry properties of the constituent semiconductors in the heterostructure. Effects such as band nonparabolicity and the infuence of remote bands on the overall energy structure are neglected *a priori*. Heterostructures whose energy structure cannot be understood on the basis of this simple parabolic model have called for more sophisticated techniques. Such methods have included the linear combination of atomic orbitals (LCAO) [4] and the envelope function approximation [5]. The envelope function approximation is based on a Kane-type analysis [6] where the symmetries of the relevant band edges are correctly taken into account. In a recent publication, Smith and Mailhiot [7] have given a generalized and rigorous treatment of the Kane-type analysis for *all* heterostructure quantum wells and superlattices. From their analysis, the plane wave matching technique can be

extracted as a special case.

In the following, we discuss a particular application of the k.p Kane theory to a simple superlattice such as (Al,Ga)As/GaAs. In the heterostructure to be discussed, the direction of the epitaxial growth is taken to be the $\hat{z}$-axis which is also the superlattice axis. Furthermore, each constituent semiconductor of the superlattice is assumed to be describable by a band model such as that shown in Fig. 6. This is a reasonable requirement because for most III-V heterostructures, the band edges that are important in optical and transport studies have the Γ_6, Γ_7 and Γ_8 symmetries at the center of the Brillouin zone.

Under flat band conditions, *i.e.*, with no applied external fields, the wavefunctions which describe the electronic carrier states in the superlattice can be written as

$$\Psi^l = \sum_j F_j^l(z) u_{j0}^l(r) \qquad (l = 1, 2) \tag{25}$$

where the $F_j^l(z)$ are the slowly varying envelope functions (slowly varying on the scale of the lattice constant) and $u_{j0}^l(r)$ describes the periodic Bloch functions at the zone center (k=0). The superscript l denotes the two semiconductors (l=1,2) which make up the alternating layers of the superlattice. Following Kane, the basis functions, u_{j0}^l's, which correspond to the Γ_6, Γ_7 and Γ_8 edges are

$$\begin{aligned}
u_{el} &= |\tfrac{1}{2}, \tfrac{1}{2}> \;=\; |S\uparrow> \\
u_{lh} &= |\tfrac{3}{2}, \tfrac{1}{2}> \;=\; \tfrac{1}{\sqrt{6}}|(X+iY)\downarrow> -2|Z\uparrow>| \\
u_{hh} &= |\tfrac{3}{2}, \tfrac{3}{2}> \;=\; \tfrac{1}{\sqrt{2}}|(X+iY)\uparrow> \\
u_{so} &= |\tfrac{1}{2}, \tfrac{1}{2}> \;=\; \tfrac{1}{\sqrt{3}}|(X+iY)\downarrow> +|Z\uparrow>|
\end{aligned} \tag{26}$$

plus the other set of four functions formed from the ones above by inversion, complex conjugation, and reversal of the spin. And as usual, the functions $|S>$, $|X>$, $|Y>$ and

$|Z>$ transform like the atomic s, p_x, p_y and p_z functions. The bulk Hamiltonian which the cell-periodic part of the Bloch states must satisfy in semiconductor l (l=1,2) is

$$H^l(k) = \frac{1}{2m}|p+\hbar k|^2 + \Delta V^l_{s,p}(z) + V(r) + \frac{\hbar}{4m^2c^2}\sigma \times \nabla V(r).[p+\hbar k| \qquad (27)$$

where $\Delta V^l_{s,p}(z)$ is the periodic potential which accounts for the conduction (valence) band discontinuity when going from semiconductor 1 to 2 in the direction of the superlattice. This Hamiltonian can be rewritten in a form which explicitly displays the k.p interaction. Taking the origin of energy to be at the bottom of the conduction band edge and E_g to be the fundamental band gap, the k.p interaction matrix formed by the 8 basis states of the Γ_6, Γ_7 and the Γ_8 subspace in semiconductor l of the superlattice, is given by:

$$\begin{pmatrix}
|\frac{1}{2},\frac{1}{2}> & |\frac{3}{2},\frac{1}{2}> & |\frac{3}{2},\frac{3}{2}> & |\frac{1}{2},\frac{1}{2}> & |\frac{3}{2},-\frac{1}{2}> & |\frac{3}{2},-\frac{1}{2}> & |\frac{3}{2},-\frac{3}{2}> & |\frac{1}{2},-\frac{1}{2}> \\
0 & \frac{2}{\sqrt{6}}Pk_z & Pk_+ & \frac{1}{\sqrt{3}}Pk_z & 0 & \frac{1}{\sqrt{3}}k_- & 0 & \frac{2}{\sqrt{6}}k_- \\
\frac{2}{\sqrt{6}}Pk_z & -E_g & 0 & 0 & \frac{1}{\sqrt{3}}Pk_- & 0 & 0 & 0 \\
Pk_- & 0 & -E_g & 0 & 0 & 0 & 0 & 0 \\
\frac{1}{\sqrt{3}}Pk_z & 0 & 0 & -E_g-\Delta^l & \frac{2}{\sqrt{6}}Pk_- & 0 & 0 & 0 \\
0 & \frac{1}{\sqrt{3}}Pk_+ & 0 & \frac{2}{\sqrt{6}}Pk_+ & 0 & \frac{2}{\sqrt{6}}Pk_z & Pk_- & \frac{1}{\sqrt{3}}Pk_z \\
\frac{1}{\sqrt{3}}Pk_+ & 0 & 0 & 0 & \frac{2}{\sqrt{6}}Pk_z & -E_g & 0 & 0 \\
0 & 0 & 0 & 0 & Pk_+ & 0 & -E_g & 0 \\
\frac{2}{\sqrt{6}}Pk_+ & 0 & 0 & 0 & \frac{1}{\sqrt{3}}k_z & 0 & 0 & -E_g-\Delta^l
\end{pmatrix} \qquad (28)$$

where Δ^l is the spin-orbit coupling [6]. The variable $k_\pm$ is defined as

$$k_\pm = \frac{k_x \pm ik_y}{\sqrt{2}} \qquad (29)$$

and

$$P = \left(\frac{-i\hbar}{m}\right) < S|p_x|X > . \qquad (30)$$

In this interaction matrix, we have neglected the kinetic energy term of $(\hbar^2k^2/2m)$ which should be added to the diagonal elements. Also not accounted for are the interactions from remote bands which would normally be handled through the Löwdin perturbation theory in typical band structure calculations (see, for example, E. O. Kane, Energy Band Theory, in *Handbook on Semiconductors*, Volume 1, ed., T. S. Moss p 193, North-Holland Publishing Co., 1982).

If the spin-orbit split-off valence band is taken to be far away from the other bands of interest at the Brillouin zone center, then its effects can be neglected and the 8×8 interaction matrix reduces to a 6×6 one. A further simplification results if the quantization of angular momentum is along the superlattice axis, *i.e.*, the $\hat{z}$-direction. In this case then $k_\parallel(k_x,k_y) = 0$. This condition decouples the $|P,M_J = \pm\frac{3}{2}>$ states from the others. The effect of this decoupling results in a dispersionless band for the $|P,M_J = \pm\frac{3}{2}>$ states. These heavy-hole states can only be correctly described by inclusion of their k.p interaction with other remote bands of the semiconductor. For our purposes here, the approximations lead to a 4×4 interaction matrix which is adequate for the description of the light particles (electrons and light-holes). This matrix, as extracted from Eq. (28) is

$$\begin{pmatrix}
|\frac{1}{2},\frac{1}{2}> & |\frac{3}{2},\frac{1}{2}> & |\frac{1}{2},-\frac{1}{2}> & |\frac{3}{2},\frac{1}{2}> \\
0 & \frac{2}{\sqrt{6}}Pk_z & 0 & 0 \\
\frac{2}{\sqrt{6}}Pk_z & -E_g & 0 & 0 \\
0 & 0 & 0 & \frac{2}{\sqrt{6}}Pk_z \\
0 & 0 & \frac{2}{\sqrt{6}}Pk_z & -E_g
\end{pmatrix} \qquad (31)$$

It is block diagonal with two identical sub-blocks describing the $|S,\pm\frac{1}{2}>$ electron and

$|P, \pm\frac{1}{2}>$ light-hole states.

6. Dispersion Relation for Superlattices

For a superlattice, the band edge discontinuities, $V_S(z)$ and $V_P(z)$, for the conduction and valence bands, respectively, become periodic with the period of the superlattice. That is to say

$$V_{S,P}(z) = 0, \qquad 0 \le z \le l_1 \tag{32}$$

$$V_{S,P}(z) = V_{S,P} \qquad l_1 \le z \le l_1 + l_2 = d \tag{33}$$

where l_1 and l_2 are the thicknesses of the layers 1 and 2 and d is the superlattice period. It therefore follows that the $F_j^l(z)$ envelope functions must obey the additional Bloch relation

$$F_j^l(z+d) = \exp(iqd) F_j^l(z) \tag{34}$$

where q is the superlattice wavevector and is restricted to the first superlattice Brillouin zone; *i.e.*,

$$|q| \le \frac{\pi}{d} \tag{35}$$

In order to determine the energy levels of the superlattice, one must solve the system of equations formed by projecting the 8×8 interaction Hamiltonian onto the j ($j = 8$) envelope functions of the superlattice. With the approximations made in the last section, the 8×8 interaction matrix was reduced to a 4×4 block diagonal system. Since the block diagonal system has 2 identical 2×2 matrices, we reduce it further to a 2×2 system.

The system of equations to be solved becomes a pair of coupled differential equations in which k_z is replaced by $(-id/dz)$. Thus, for the envelope functions $F_S^l(z)$ and $F_P^l(z)$ associated with the conduction and the light-hole valence bands, the 2×2 system derived from Eq. (31) is (*cf.* Ref.[5])

$$\begin{pmatrix} V_S^l(z) - E & -i\frac{2}{\sqrt{6}}P^l\frac{d}{dz} \\ -i\frac{2}{\sqrt{6}}P\frac{d}{dz} & -E_g + V_P^l(z) - E \end{pmatrix} \begin{pmatrix} F_S^l(z) \\ F_P^l(z) \end{pmatrix} = 0 \tag{36}$$

where E is the eigen-energy and we have also added the band discontinuity $V_{S,P}^l(z)$. For the light-hole valence band alone, the equation to be solved is obtained by eliminating $F_S^l(z)$ above. The result is

$$\left\{\frac{2}{3}P^2\frac{d}{dz}\left[\frac{1}{V_S^l(z) - E}\right]\frac{d}{dz} + (V_P(z) - E_g)\right\} F_P^l(z) = EF_P^l(z). \tag{37}$$

The function $F_P^l(z)$ is required to be continuous across the hetero-interface between the two semiconductors and so is its derivative. The derivative condition is derived from Eq. (37) by integrating it across the interface to give

$$\left[\frac{1}{V_S^{(1)} - E}\right]\frac{dF_P^{(1)}}{dz} = \left[\frac{1}{V_S^{(2)} - E}\right]\frac{dF_P^{(2)}}{dz}. \tag{38}$$

The Bloch and the boundary conditions yield a 4×4 homogeneous determinant whose solution is nonzero if the relationship

$$\cos k_1 l_1 \cos k_2 l_2 - \frac{1}{2}\left[\eta + \frac{1}{\eta}\right]\sin k_1 l_1 \sin k_2 l_2 = \cos qd \tag{39}$$

holds where

$$\eta = \frac{k_1}{k_2}\left(\frac{E + E_g - V_P}{E + E_g}\right). \tag{40}$$

The wavevectors k_1 and k_2 are to be determined from the dispersion relationships obtained from the Kane 8 × 8 interaction matrix of Eq. (28). This dispersion relationship is of the Kronig-Penney type and is in its most general form. The wavevectors are to be modified in layer 1 or 2 depending on whether the wavefunction is standing or evanescent in that layer. This change would simply convert some of the trignometric functions into hyperbolic sine or cosine. In the limit that the layer with the larger band gap is many times thicker than that with the smaller band gap, the single quantum well result obtained earlier is recovered.

In order to treat the heavy-hole band correctly, the complete Smith-Mailhiot [7] model must be used. Our purpose here, however, has been to illustrate an approximate method derived from the rigorous k.p theory. For a simple (Al,Ga)As/GaAs superlattice, for example, the host semiconductors have wide band gaps and the eigen-energies, $E \ll E_g$, and in the two-band Kane model, the derivative continuity condition becomes

$$\frac{1}{m_1}\frac{dF_P^{(1)}}{dz} = \frac{1}{m_2}\frac{dF_P^{(2)}}{dz}, \tag{41}$$

which is the condition generally assumed in the simple particle-in-the-box model. In this case k_1 and k_2 take on the expressions of Eqs. (8) and (5); the parameter η then becomes

$$\eta = \frac{m_1 k_2}{m_2 k_1}. \tag{42}$$

The model we have been discussing is adequate for an understanding of lattice-matched heterostructures. When the structures are not lattice-matched then the relevant Hamiltonian must be modified. In the next section we discuss lattice-mismatched structures and the effect of mismatch-induced strain on the band stucture.

7. Strained-Layer Heterostructures

In the past, most heterostructure work has emphasized structures made from semiconductors of almost the same lattice parameter but different band gaps. In this way, interesting materials properties and new devices have been made. The important ingredient in this kind of work has been the minimization of lattice strain by lattice-matching, *i.e.*, the materials involved must have the same size unit cells and usually similar coefficients of thermal expansion so that lattice strains are not introduced into the resulting heterostructure upon cooling the sample from the fabrication temperature to room temperature.

The restrictions imposed by the lattice-matching condition, however, have limited the range of materials and materials properties that can be engineered from semiconductors with comparable lattice constants. The trend in recent years has therefore been to remove the arbitrary restriction of lattice-matching by allowing materials of widely differing lattice constants to be fabricated into a new breed of heterostructures called the *strained-layer superlattices* (SLS's). These superlattices are mismatched systems similar in style to the ones discussed previously. The major difference is that the lattice-mismatch is accomodated totally by a uniform lattice strain. One of the provisions for this to happen without the deleterious effects of misfit dislocations is that the hetero-epitaxial layers comprising the superlattice be of a certain dimension. If this criterion is satisfied, SLS's of high quality can be prepared from layers with lattice-mismatches of up to 7% [8,9]. The freedom of choice of the SLS materials and the interesting effects of elastic layer strains allow SLS stuctures to exhibit a wide range of tailorable properties which are of scientific and technological interest.

Some of the SLS's that have been fabricated include those with materials from: (1)

the group IV elements of Si and Ge [10], (2) some III-V compound semiconductors with other III-V materials or with II-VI materials [11].

The choice of suitable material combinations depends on some factors such as: (1) compatibility of the materials in the epitaxial growth process, (2) mechanical stability and (3) thermal conductivity match.

Perhaps an important consideration for the SLS's of the group III-V and IV semiconductors is that the interatomic bonding distances (better expressed as the tetrahedral covalent radius, TCR) are very similar. These distances are within 15% of the average value for the atomic numbers $13 \leq Z \leq 51$. This information is readily available from any good Periodic Table. See Table 2.

Table 2: Tetrahedral covalent radii (TCR) for some group III, IV and V elements.

Atomic No. Z	13	14	15	31	32	33	49	50	51
Element	Al	Si	P	Ga	Ge	As	In	Sn	Sb
TCR (Å)	1.18	1.11	1.06	1.26	1.22	1.20	1.44	1.41	1.40

The close similarity of these elements is one of the factors which makes them epitaxially compatible.

8. Tetragonal Distortion

In very simple terms, the idea behind the growth of strained-layer superlattices is that an alternating sequence of heterostructure layers with differing lattice constants be deposited one on top of the other such that the lattice-mismatch stress is accommodated *elastically* without the generation of misfit dislocations. For layer thicknesses within a characteristic

dimension, h_c, the layers with larger lattice parameter than the substrate will be in compression while those with smaller lattice parameter will be in tension.

The success of the fabrication of most SLS's has depended on the effect of tetragonal distortion due to the existence of two-dimensional (biaxial) stress on the crystals. This effect, also called the Poisson effect, causes layers to be expanded or compressed in the direction perpendicular to the interfacial planes. Such a process is demonstrated in Fig. 7. Notice that the layer on top, the epi-layer, has been stretched in the vertical direction. The vertical lattice-mismatch is $\Delta a_\perp / a_s = (a_\perp - a_s)/a_s$. This is to be contrasted with the normal lattice-mismatch defined as $\Delta a / a_s = (a_f - a_s)/a_s$. For cubic crystals oriented in the [001] direction, the two lattice-mismatches are related by the simple result that

$$\frac{\Delta a}{a_s} = \frac{C_{11}}{C_{11} + 2C_{12}} \left(\frac{\Delta a_\perp}{a_s} \right) \tag{43}$$

where the C_{ij} are the well known elastic constants from elementary elasticity theory [12].

The field of strained-layer epitaxy was pioneered by Matthews and Blakeslee who grew layers composed of the Ga(As,P)/GaAs material system [13,14,15]. They demonstrated that it was possible to grow dislocation-free layers from mismatched semiconductors as long as the layer thicknesses were kept below a certain critical dimension given by

$$h_c = \frac{b(1 - \nu \cos^2 \alpha)}{2\pi f (1 + \nu) \cos \lambda} \left[\ln \left(\frac{h_c}{b} \right) + 1 \right] \tag{44}$$

where ν is Poisson's ratio, α is the angle between the Burgers vector b and the length of the dislocation line that lies in the interfacial plane and λ is the angle between b and that direction in the interface that is perpendicular to the intersection of the slip plane and the interface, f is the unstrained lattice-mismatch between the two layers. For layer thicknesses less than h_c, wafers without misfit dislocations can be grown.

The strained-layer superlattices that are prevalent today are prepared by the advanced crystal growth techniques of molecular beam epitaxy (MBE) [16,1] and metal-

organic chemical vapor deposition (MOCVD) [17]. They consist, in the main, of two semiconductors of different lattice constants grown alternately on a substrate. For the $GaAs_xP_{1-x}/GaP$ material system, for example, an epitaxy initiation layer composed of a graded layer is first grown on the GaP substrate. The $GaAs_xP_{1-x}$ layer deposited on the GaP substrate is then graded from $x = 0$ to some value of x where the superlattice is to start. Schematically, the superlattice structure would look like the illustration shown in Fig. 8. For different compositions of x in the SLS, the lattice constant of the strained layers in the planes parallel to the interfaces, $a_\parallel$, would be given by [15]

$$a_\parallel = a_1 \left[1 + \frac{f}{1 + (G_1 h_1 / G_2 h_2)}\right] \tag{45}$$

and

$$a_\parallel = a_2 \left[1 - \frac{f}{1 + (G_2 h_2 / G_1 h_1)}\right] \tag{46}$$

where a_1 and a_2 are the unstrained lattice constants of the alternating layers 1 and 2 in the SLS; G_i and h_i are, respectively, the shear moduli and layer thicknesses of the layers i (i =1, 2) and f is the lattice mismatch ($\Delta a/a$) of the unstrained layers. From these relations, it can be seen that the thinner of the two layers experiences the greater strain (this fact is also intuitively obvious).

9. Energy Structure of Strained Layers

One of the most interesting effects of the strain-stress interaction in a semiconductor heterostructure is the modification of the energy band structure. It is important to understand this modification because ultimately, the other materials properties depend on it. It is a well-documented fact that the application of a uniaxial stress to semiconductor crystals such as Si and GaAs removes the cubic symmetry and lifts some of the degeneracy at the valence band [18].

We use, as an example, the strained-layer heterostructure that is formed by the deposition of (Ga,In)P on a GaAs substrate. The GaAs substrate has a lattice constant of 5.6534 Å which is smaller than that of the (Ga,In)P. The layer thickness of the (Ga,In)P on top of the GaAs is chosen such that the lattice mismatch is completely accommodated by biaxial elastic strain. For a quantitative analysis of the energy structure of this heterostructure, we choose the $\hat{z}$-axis to be in the [001] crystallographic direction. The substrate plane is then that of the (001) surface. Olsen *et al.* [19] have done some experimental work on the effect of elastic strain on the band gap of (Ga,In)P when it is grown lattice-mismatched on a GaAs substrate. It was noted earlier that the effect of a "biaxial compressive" stress on the unit cell of a crystal was to tetragonally distort the cell as shown in Fig. 7(b). The effect of this compressive stress on the valence band is to lift the energy degeneracy at k=0. This is shown in Fig. 9.

In a zinc blende material structure such as the (Ga,In)P/GaAs system, the valence band edge at k=0 would have been a multiplet with a sixfold degeneracy of orbital symmetry Γ_{15} without the spin-orbit interaction. With the spin-orbit interaction, however, the degeneracy is lifted into a fourfold $p_{3/2}$ multiplet (J=3/2, m_J=±3/2, ±1/2) and a $p_{1/2}$ multiplet (J=1/2, m_J=±1/2). This is shown in Fig. 9(a). The introduction of stress into the material results in the further lifting of the remaining degeneracy as shown in Fig. 9(b). The interaction of the strain and the orbital effects on the valence band $p_{3/2}$ state can be described by a Hamiltonian. Hamiltonians constructed to describe strain effects have been discussed in previous work [20,21,22]. These Hamiltonians are normally expressed in terms of the angular momentum operator J (J=3/2). The most convenient description for our purposes here is the Hamiltonian given by

$$\begin{aligned} H_{st} \quad &= -a(\epsilon_{xx} + \epsilon_{yy} + \epsilon_{zz}) - 3b[(J_x^2 - J^2/3)\epsilon_{xx} + (J_y^2 - J^2/3)\epsilon_{yy} \\ &+ (J_z^2 - J^2/3)\epsilon_{zz} - (6d/\sqrt{3})[\{J_x J_y\}\epsilon_{xy} + \{J_x J_z\}\epsilon_{xz} + \{J_y J_z\}\epsilon_{yz}] \end{aligned} \tag{47}$$

where the ϵ_{ij} are the ordinary components of the strain tensor, the factors $\{J_xJ_y\}$, *etc.*, represent the symmetrized products of $\{J_xJ_y\}=\frac{1}{2}(J_xJ_y + J_yJ_x)$. The parameter a is the hydrostatic deformation potential. The other parameters, b and d, represent the shear deformation potentials appropriate to the strain for tetragonal or rhombohedral symmetry, respectively.

In the (Ga,In)P epitaxial layer on a [001]-oriented GaAs substrate, with which we are concerned here, the lattice-mismatch is accommodated by a uniform biaxial stress parallel to the [100] and [010] directions. The planar elastic strain components, therefore, are given by

$$\epsilon_{xx} = \epsilon_{yy} = -\epsilon_{\parallel}. \tag{48}$$

The strain is defined as negative ($-\epsilon$) in this case because the parallel lattice constant, $a_{\parallel}$, for the epilayer is smaller than the substrate lattice parameter. Our choice of $\hat{\mathbf{z}}\|[001]$ results in a diagonal strain tensor, ϵ_{ij}. The off-diagonal terms of the strain tensor are zero, *i.e.*,

$$\epsilon_{xy} = \epsilon_{yz} = \epsilon_{xz} = 0. \tag{49}$$

An immediate consequence of this result is that the term in the Hamiltonian representing the rhombohedral shear deformation vanishes. From ordinary elasticity theory, one can write down a specific stress-strain ($\sigma - \epsilon$) relationship for the case under discussion. Because of the symmetry of cubic crystals, the generalized stress-strain relationship of

$$\sigma_i = C_{ij}\epsilon_j \tag{50}$$

can be simplified to

$$\begin{pmatrix} \sigma_{xx} \\ \sigma_{yy} \\ 0 \\ 0 \\ 0 \\ 0 \end{pmatrix} = \begin{pmatrix} C_{11} & C_{12} & C_{12} & 0 & 0 & 0 \\ C_{12} & C_{11} & C_{12} & 0 & 0 & 0 \\ C_{12} & C_{12} & C_{11} & 0 & 0 & 0 \\ 0 & 0 & 0 & C_{44} & 0 & 0 \\ 0 & 0 & 0 & 0 & C_{44} & 0 \\ 0 & 0 & 0 & 0 & 0 & C_{44} \end{pmatrix} \begin{pmatrix} \epsilon_{xx} \\ \epsilon_{yy} \\ \epsilon_{zz} \\ 0 \\ 0 \\ 0 \end{pmatrix} \tag{51}$$

where we have used the additional simplification that the stress is biaxial and the fact that the strain tensor is diagonal beacause of our choice of the $\hat{\mathbf{z}}$-axis. From the stress-strain equation above one can extract the result

$$\epsilon_{zz} = -\frac{2C_{12}}{C_{11}}\epsilon_{xx} = \frac{2C_{12}}{C_{11}}\epsilon_{\parallel}. \tag{52}$$

Substituting the elastic strains of Eqs. (48), (49), and (52) into Eq. (47), we obtain the resultant strain Hamiltonian,

$$H_{st} = 2a\left(\frac{C_{11} - C_{12}}{C_{11}}\right)\epsilon_{\parallel} - 3b\left(\frac{C_{11} + 2C_{12}}{C_{11}}\right)(L_z^2 - \frac{L^2}{3})\epsilon_{\parallel} \tag{53}$$

where the first term represents the shift of the band gap due to the strain; the second term is the linear splitting of the $p_{3/2}$ multiplet. We take the wave functions for the valence band states in the $|J, m_J>$ momentum representation. Referred to the [100] direction, the unperturbed wave functions of both the valence and the conduction bands

which will diagonalize the strain Hamiltonian of Eq. (53) are given by

$$\begin{aligned} u_{sl} &= |\tfrac{1}{2},\tfrac{1}{2}>_{100} = |S\uparrow> \\ u_{lh} &= |\tfrac{3}{2},\tfrac{1}{2}>_{100} = \sqrt{1/3}|\sqrt{1/2}|(Y+iZ)\downarrow> -\sqrt{2}X\uparrow|> \\ u_{hh} &= |\tfrac{3}{2},\tfrac{3}{2}>_{100} = \sqrt{1/2}|(Y+iZ)\uparrow> \\ u_{so} &= |\tfrac{1}{2},\tfrac{1}{2}>_{100} = \sqrt{1/3}||(Y+iZ)\downarrow> +X]\uparrow> \end{aligned} \tag{54}$$

where $\uparrow$ and $\downarrow$ indicate spin up and spin down. $|X>$, $|Y>$ and $|Z>$ are, again, the orbital wave functions for the valence band with tetrahedral symmetry similar to the atomic p functions. The function $|S>$ is the conduction band wave function which transforms like the atomic s function. We have only considered states with positive m_J here [23] (see C. Kittel, *Quantum Theory of Solids*, J. Wiley & Sons, Inc., N. Y., p 282 1963). The eigen-energies of the perturbed bands are obtained by writing down the Hamiltonian matrix from Eqns. (53) and (54) and diagonalizing it. With these eigen-energies, the energy difference between the conduction and valence bands at k=0, can be given, to first order in the strain as [24,25]

$$\Delta E_0(1) = \left[-2a\left(\frac{C_{11}-C_{12}}{C_{12}}\right) + b\left(\frac{C_{11}+2C_{12}}{C_{11}}\right)\right]\epsilon_{\parallel} \tag{55}$$

$$\Delta E_0(2) = \left[-2a\left(\frac{C_{11}-C_{12}}{C_{12}}\right) - b\left(\frac{C_{11}+2C_{12}}{C_{11}}\right)\right]\epsilon_{\parallel} \tag{56}$$

$$\Delta(E_0+\Delta_0) = -2a\left(\frac{C_{11}-C_{12}}{C_{11}}\right)\epsilon_{\parallel} \tag{57}$$

According to these equations the change in the fundamental band gap, $\Delta E_0(1)$, is a linear function of the strain (to first order). In the experimental results reported by Olsen *et al.* [19], several strained-layer heterostructures of $Ga_{0.5}In_{0.5}P/GaAs$ showed a linear band gap shift with strain. If the parameters in Eq. (53) are known for this material, the quantitative results can be compared with experiment. Up to this point, we have discussed the effect of the strain on a single epitaxial layer on a lattice-mismatched

substrate. In a normal strained-layer superlattice, two semiconductors of different band gaps are alternately deposited one on top of the other. We consider in this last part of the discussion, another common combination of materials for SLS's: the $In_xGa_{1-x}As/GaAs$ system. $In_xGa_{1-x}As$ has a smaller band gap than GaAs; but it has a larger lattice constant than GaAs. In the $In_xGa_{1-x}As/GaAs$ SLS, the $In_xGa_{1-x}As$ is under compression. Its band gap will increase with respect to the bulk value. The valence band degeneracy will be lifted and the heavy- and light-hole bands separated. The GaAs layers on the other hand, are under biaxial tension. The band gap of these layers will decrease because of the tension. In addition to this, the light-hole band moves toward the conduction band, reversing position with the heavy-hole band. The quantitative description of the changes in the band gaps is still given by the Eqns. (55), (56) and (57). The elastic strain constant, ϵ, is now either negative or positive depending on whether the layer is in biaxial compression or tension. Fig. 10 shows a schematic illustration of the effect of planar biaxial compression and tension on the band structure of a direct gap semiconductor.

The energy structure of a strained-layer superlattice can be calculated by using a tight binding model. The tight binding parameters for the alloy semiconductors would be obtained by taking weighted averages of the constituent binary compounds. In this case it would be the compounds of InAs and GaAs in the $In_xGa_{1-x}As/GaAs$ SLS's.

An alternative approach is to use the envelope function approximation discussed earlier in the context of the unstrained superlattices. The modification one would have to make is to include in the Hamiltonian a term for the strain. Such a term would be the strain Hamiltonian given in Eq. (47). The complete Hamiltonian that would be used in the calculation of the band structure for a strained layer superlattice would be

$$H = H_0 + H_{so} + H_{st} \tag{58}$$

where H_0 is the Hamiltonian in the single particle approximation including the periodic potential discontinuity between the layers, H_{so} is the spin-orbit Hamiltonian and H_{st} is the strain Hamiltonian given above. In principle, then, the band structure of SLS's can be solved by using the envelope function approximation within the k.p framework once the Hamiltonian has been determined.

High quality strained-layer superlattices of $In_xGa_{1-x}As/GaAS$ have been fabricated [27]. Fig. 11 shows the photoluminescence spectra obtained for $x \approx 0.2$; the $In_{0.2}Ga_{0.8}As$ quantum wells are $\sim$ 38 Å and the GaAs barriers are varied from 30 Å to 90 Å. Notice how the peak emission shifts to higher energy with increasing barrier thickness. This is a result of the combined effect of size quantization and biaxial strain.

In this work we have discussed the basic physics of SLS's including the relevant quantitative relations. The experimental aspects of these structures can be found in some of the literature cited and the references therein.

10. Acknowledgement

The author acknowledges Dr. G. Dresselhaus and Prof. S. Kim for their editorial review of the manuscript and thanks Profs. R. B. Adler and C. G. Fonstad for support.

References

[1] L. L. Chang and Ploog (eds.), *Molecular Beam Epitaxy*, NATO Advanced Science Institute Series, M. Nijhoff Publishers, Dordrecht (1985).

[2] W. Jones and N. H. March, *Theoretical Solid State Physics*, Vol. 1, p 27, Wiley-Interscience, N.Y. (1973).

[3] G. A. Sai Halsz, R. Tsu and L. Esaki, Appl. Phys. Lett., **30**, 651 (1977).

[4] G. A. Sai Halasz, L. Esaki and W. A. Harrison, Phys. Rev., **B18**, 2812 (1978).

[5] G. Bastard, Phys. Rev., **B24**, 5693 (1981).

[6] E. O. Kane, J. Phys. Chem. Solids, **1**, 249 (1957).

[7] D. L. Smith and C. Mailhiot, Phys. Rev., **B12**, 8345 (1986).

[8] E. Kasper and H. J. Herzog, Thin Solid Films, **44**, 357 (1977).

[9] G. C. Osbourn, J. Appl. Phys., **53**, 1586 (1982).

[10] R. People, IEEE J. Quant. Electronics, **QE22**, 1697 (1986).

[11] G. C. Osbourn, IEEE J. Quant. Electronics, **QE22**, 1677 (1986).

[12] A. G. Guy, *Introduction to Materials Science*, Chapter 9, McGraw-Hill, (1972).

[13] J. W. Matthews and A. E. Blakeslee, J. Cryst. Growth, **27**, 118 (1973).

[14] J. W. Matthews and A. E. Blakeslee, J. Cryst. Growth, **29**, 273 (1975).

[15] J. W. Matthews and A. E. Blakeslee, J. Cryst. Growth, **32**, 265 (1976).

[16] A. Y. Cho, Progress in Solid State Chemistry, **10**, 157 (1975).

[17] P. D. Dapkus, Ann. Rev. Mater. Sci. Vol. **12**, 243 (1982).

[18] F. Pollak and M. Cardona, Phys. Rev., **172**, 816 (1968).

[19] G. H. Olsen, C. J. Nuese and R. T. Smith, J. Appl. Phys., **49**, (1978).

[20] G. E. Pikus and G. L. Bir, Sov. Phys. Solid State, **1**, 136 (1959).

[21] G. E. Pikus and G. L. Bir, Sov. Phys. Solid State, **1**, 1502 (1960).

[22] W. H. Kleiner and L. M. Roth, Phys. Rev. Lett., **2**, 334 (1959).

[23] C. Kittel, *Quantum Theory of Solids*, J. Wiley & Sons, Inc., N. Y. (1963).

[24] A. Gavin and M. Cardona, Phys. Rev. **B1**, 672 (1970).

[25] H. Asi and K. Oe, J. Appl. Phys., **54**, 2052 (1983).

[26] G. C. Osbourn, J. Vac. Sci. Technol., **B1**, 379 (1983).

[27] J. M. Gibson and R. Dawson (eds.), *Materials Res. Society, Symposia Proceedings*, Vol. **37**, 223 (1985).

Figure Captions

Figure 1: Configuration of a single GaAs quantum well sandwiched between two (Al,Ga)As confining layers.

Figure 2: Schematic energy band diagram of a single (Al,Ga)As/GaAs/(Al,Ga)As single quantum well in both the conduction and valence bands.

Figure 3: A graphical solution of the eigen-value equation for the even carrier states in a single (Al,Ga)As/GaAs/(Al,Ga)As single quantum well.

Figure 4: Room temperature photoluminescence spectrum of a multiple quantum well (Al,Ga)As/GaAs/(Al,Ga)As structure and that of a bulk GaAs crystal.

Figure 5: Band diagram of a single and multiple (Al,Ga)As/GaAs/(Al,Ga)As quantum well system showing the character of the allowed optical transitions. Also shown in (b) are the transitions in a bulk GaAs crystal.

Figure 6: Band structure of a III-V compound semiconductor (*e.g.* (Al,Ga)As or GaAs) in the vicinity of the Brillouin zone.

Figure 7: Schematic representation of the strain effect of tetragonal distortion of a unit cell of a lattice.

Figure 8: Schematic illustration of a strained-layer superlattice (after Osbourn [9]).

Figure 9: Effects of compressive stress on the bands of GaAs (adapted from Pollak and Cardona [18]).

Figure 10: Effects of planar biaxial compression and tension on the band structure of a III-V compound semiconductor (*e.g.* GaAs).

Figure 11: Photoluminescence spectra of $In_xGa_{1-x}As/GaAs$ SLS's with $x \sim 0.2$. The $In_xGa_{1-x}As$ layer is ~38 Å. The GaAs thickness is varied as shown (after Anderson *et al.* in [27]).

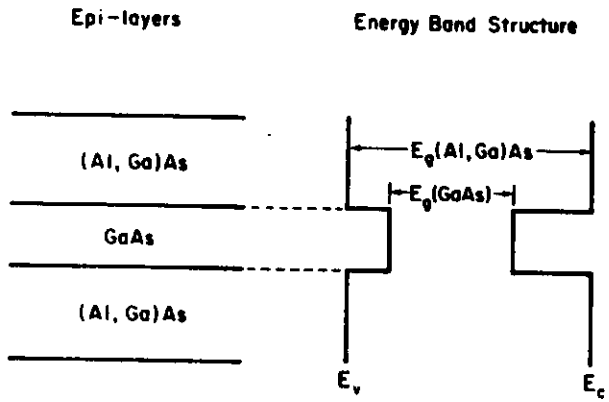

Figure 1

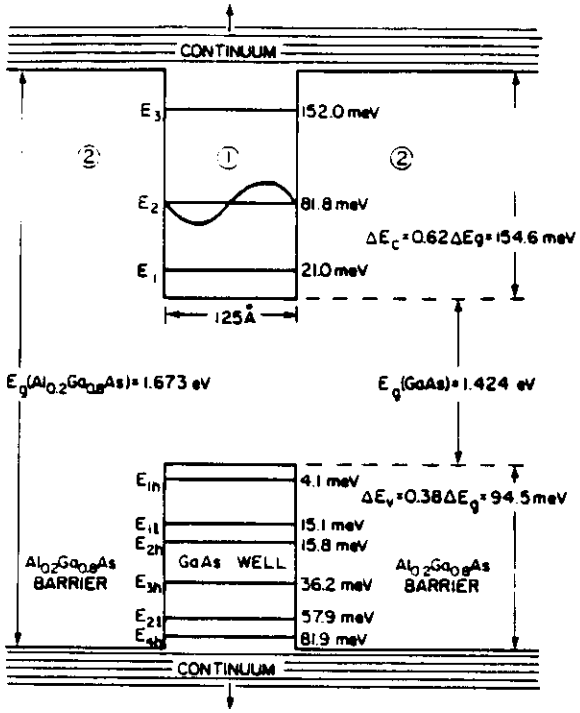

Figure 2

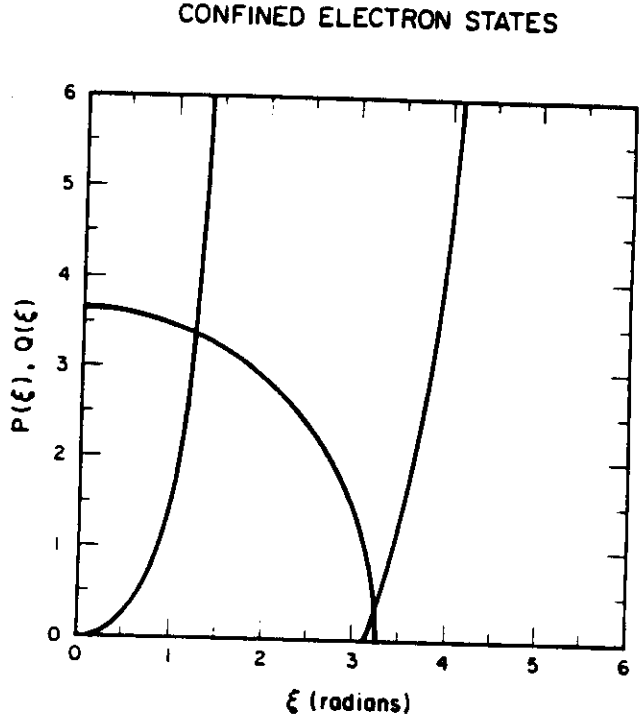

Figure 3

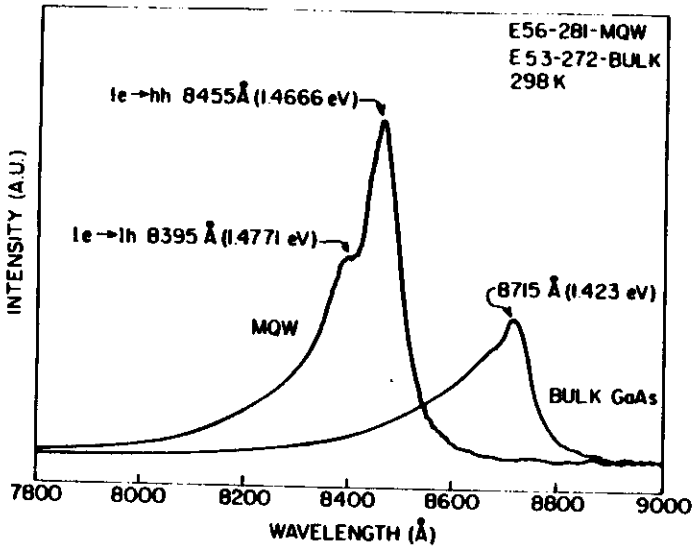

Figure 4

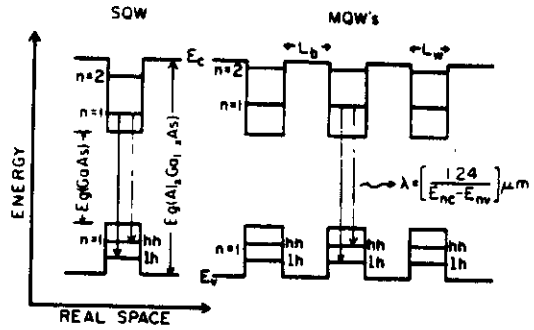

(a) SQW and MQW's Optical Transitions

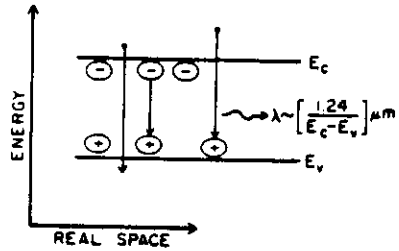

(b) Bulk $Al_xGa_{1-x}As$ Optical Transitions

Figure 5

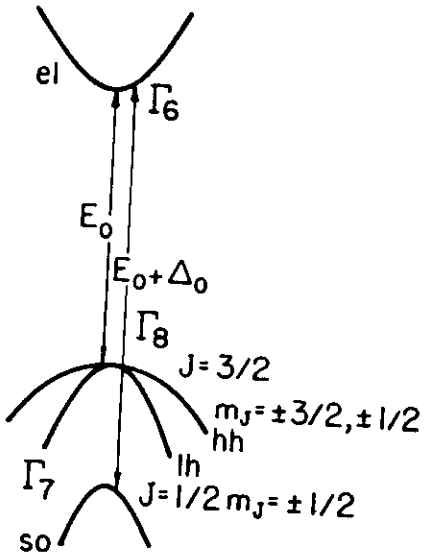

Figure 6

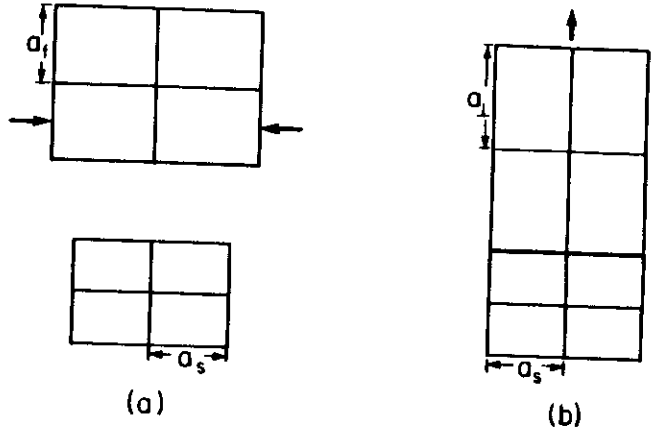

Figure 7

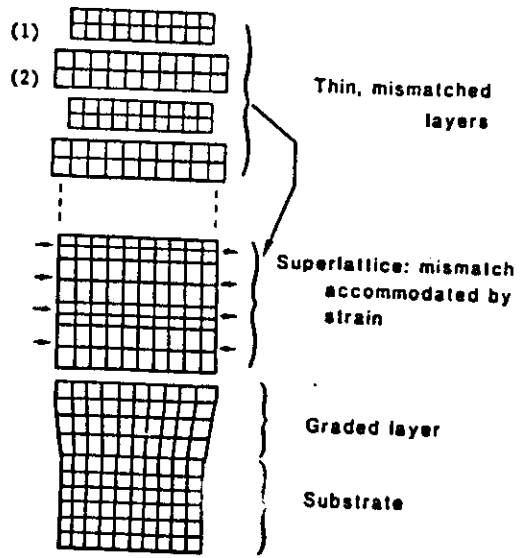

Figure 8

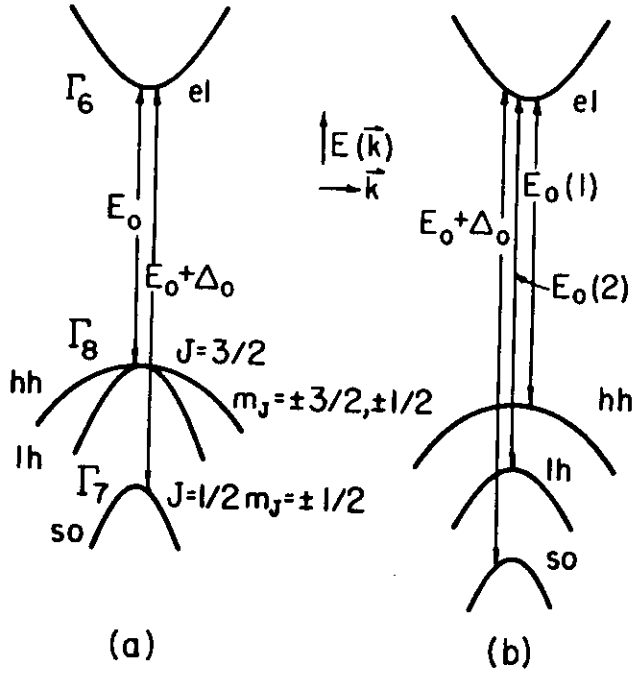

Figure 9

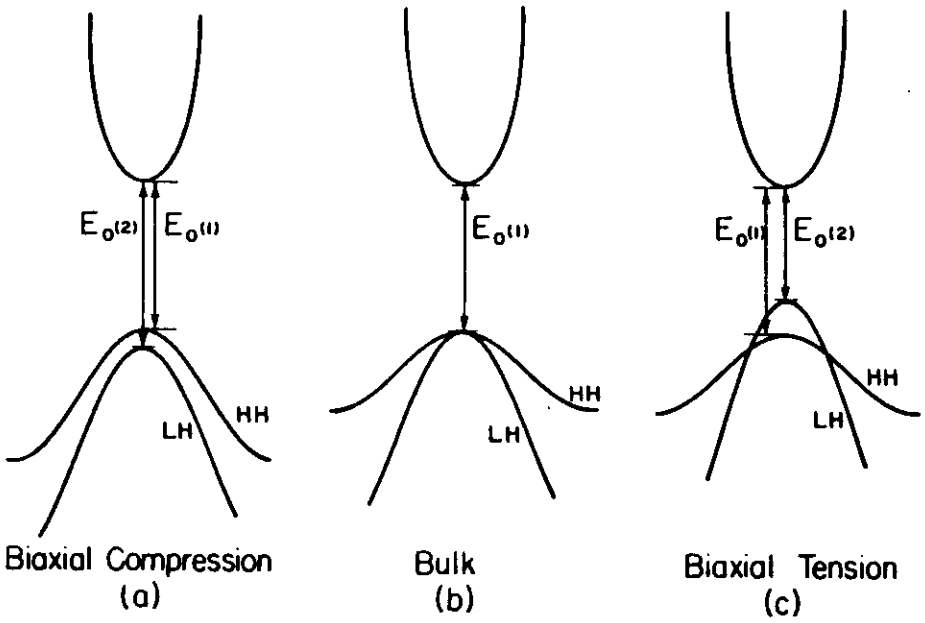

Figure 10

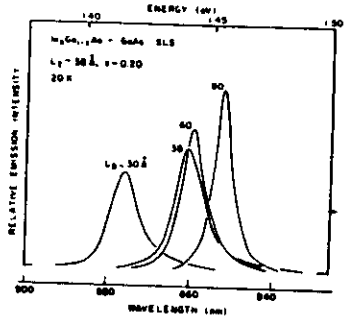

Figure 11